ISSN 0869-5911, Petrology, 2019, Vol. 27, No. 4, pp. 425–437. © Pleiades Publishing, Ltd., 2019.

The Timing of the Paleo-Asian Oceanic Closure: Geochemical Constraints from the Jigede Gabbro in the Alxa Block

Zheng Liu[a], Xin Zhang[b], Shu-Cheng Tan[a, *], Xin Sha[c], Xiao-Hu He[a], and Qing Zhou[d]

[a]*School of Resource Environment and Earth Science, Yunnan University, Kunming, 650091 China*
[b]*College of Resources and Environmental Science, Ningxia University, Yinchuan, 750000 PR China*
[c]*College of Earth Sciences, Guilin University of Technology, Guilin, 541004 PR China*
[d]*Chengdu Center, Chinese Geological Survey, Chengdu, 610081 PR China*
**e-mail: tansc001@126.com*

Received September 21, 2018; revised February 18, 2019; accepted May 8, 2019

Abstract—This paper investigates the Jigede gabbros from the Shalazhashan tectonic belt, Alxa Block. Laser ablation-inductively coupled plasma-mass spectrometry (LA-ICP-MS) zircon U-Pb dating reveals that they were emplaced in the Middle Permian (ca. 262 Ma). All the gabbro samples collected from the intrusion exhibit low contents of TiO_2 (0.24–0.37 wt %) and $Fe_2O_3^T$ (4.87–5.41 wt %), but high levels of MgO (11.15–12.15 wt %), CaO (11.45–12.75 wt %), Al_2O_3 (14.18–17.08 wt %) and high Mg# (0.81–0.83). Relative to HREEs and LILEs, the gabbros are enriched in LREEs and depleted in Th, Nb, Ce, Zr, Hf, and Ti, with positive Eu, Sr and U anomalies. In contrast to MORB, the Jigede intrusion has higher initial $^{87}Sr/^{86}Sr$ values of 0.7046 to 0.7054 and lower $\varepsilon_{Nd}(T)$ of + 1.8 to + 4.8. Elemental and isotopic data suggest that the intrusion was likely to have been produced by partial melting of a shallow lithospheric mantle source modified by slab-derived fluids, with subsequent cumulation of plagioclase. Thus, the Jigede intrusion was emplaced in a back-arc setting, in response to the Paleo-Asian oceanic subduction. In addition, the final closure of the Paleo-Asian Ocean did not occur prior to the Middle Permian.

Keywords: Permian, Gabbro, Lithospheric mantle, Alxa Block, Paleo-Asian ocean

DOI: 10.1134/S0869591119040076

INTRODUCTION

The Central Asian Orogenic Belt (CAOB) has long been considered as one of the largest accretionary orogens consisting of island arcs, ophiolitic belts, accretionary complexes, and Precambrian terranes (Kozakov et al., 1976, 1999; Sengör et al., 1993; Kovach et al., 2004; Windley et al., 2007; Kröner et al., 2014; Kozakov and Azimov, 2017). Accompanied by the southward subduction and closure of the Paleo-Asian Ocean, extensive continental growth occurred in the CAOB from Neoproterozoic to Mesozoic (Khain et al., 2003; Jahn et al., 2004; Windley et al., 2007; Kröner et al., 2014, 2017; Xiao et al., 2015). However, there is currently no consensus on the timing of the final closure of the Paleo-Asian Ocean, with different studies placing the estimate from Late Devonian to Late Triassic (Jahn et al., 2004; Xiao et al., 2009; 2015; Windley et al., 2007; Han et al., 2011; Kröner et al., 2014, 2017; Zhang et al., 2015a, 2015b).

The CAOB is located to the south of the Siberia-East Europe cratons and the north of the Tarim-Alxa-North China Cratons (Fig. 1a). It is generally accepted that the Paleo-Asian Oceanic closure is recorded by the Tianshan-Solonker suture zones, which extend along the northern edges of the Tarim-Alxa-Tarim cratons (Xiao et al., 2015). The Alxa is a key junction between the Tarim and the North China, with the former to its west and the latter to its east (Fig. 1a). Compared to its two flanking geographical neighbors, the Alxa Block has received significantly less research attention. One of the geological features of the Alxa Block is the presence of abundant late Paleozoic to Mesozoic igneous rocks, which mostly comprise granitoids, and to a lesser extent, mafic to intermediate intrusions, with a small proportion of lava (Liu et al., 2017a, 2017b; Fig. 1b). These igneous rocks could offer important insights into the tectonic evolution of the Paleo-Asian Ocean as a record of its southward subduction process. However, previous studies have focused on crust-derived granitoids and less attention has been paid to mantle-derived basaltic rocks.

In this paper, we investigate the Jigede gabbro intrusion from the Shalazhashan tectonic belt in the northern Alxa Block. New laser ablation–inductively coupled plasma–mass spectrometry (LA-ICP-MS) zircon U-Pb dating, whole-rock geochemical and Sr-

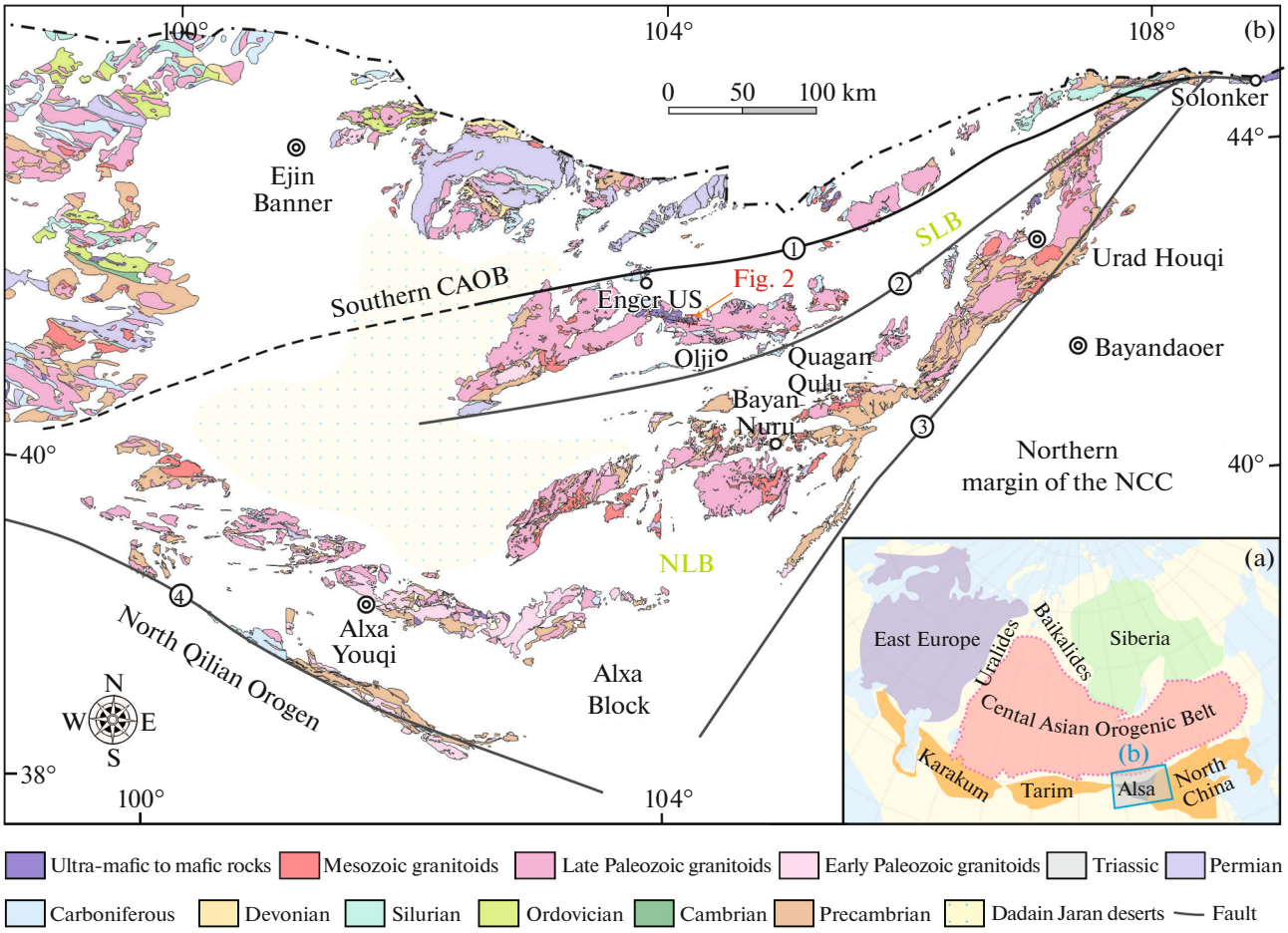

Fig. 1. (a) Simplified tectonic sketch map of the Central Asian Orogenic Belt (CAOB), showing the Location of the Alxa Block (modified after Liu et al. (2017a, 2017b)). (b) Geological map of the Alxa Block (modified after Liu et al. (2017a, 2017b)). SLB – Shalazhashan belt; NLB – Nuru-Langshan belt; ① – Enger Us fault; ② – Badain Jaran fault; ③ – Langshan fault; ④ – Longshoushan Fault.

Nd isotopic data of the intrusion are obtained to explore its petrogenesis and the associated tectonic setting. These results were subsequently used to constrain the timing of the final closure of the Paleo-Asian Ocean.

GEOLOGICAL CONTEXT AND SAMPLING

The Alxa Block is separated from the southernmost CAOB by the Enger Us fault (Fig. 1b). The Enger Us ophiolite suite distributed along the fault, represents the site of the final Paleo-Asian oceanic closure in the Alxa area (Wang et al., 1994; Zheng et al., 2014). The Alxa Block is divided by the Badain Jaran fault into two tectonic belts, including the Shalazhashan belt in the north and the Nuru-Langshan belt in the south (Fig. 1b). The Quagan Qulu ophiolite suite along the fault was produced in a back-arc setting, in response to the Paleo-Asian oceanic subduction (Wang et al., 1994; Wu et al., 1998; Zheng et al., 2014). The Alxa Block is underlain by Precambrian rocks and Late Paleozoic strata, with the absence of Early Paleozoic strata (Fig. 1b). There are abundant Paleozoic to Mesozoic magmatic rocks in the block, including predominant granitoids and secondary mafic-intermediate intrusions as well as lavas (Fig. 1b).

The magmatic rocks in the Shalazhashan tectonic belt are dominated by late Paleozoic to Triassic granitoids (301 to 247 Ma), with minor amounts of diorites and gabbros (264 to 249 Ma) (Liu et al., 2017a, 2017b). The strata in the belt is composed mainly of late Paleozoic sedimentary rocks represented by the Late Carboniferous to Early Permian Amushan Formation. The Amushan Formation can be subdivided into a lower sequence of lava-interbedded clastic rocks with zircon U-Pb ages of 320 to 302 Ma, and upper sequences of shale, sandstone, and conglomerate (Lu et al., 2012; Liu et al., 2017a, 2017b).

In this contribution, we investigate the Jigede intrusion, which was emplaced in a Permian granite

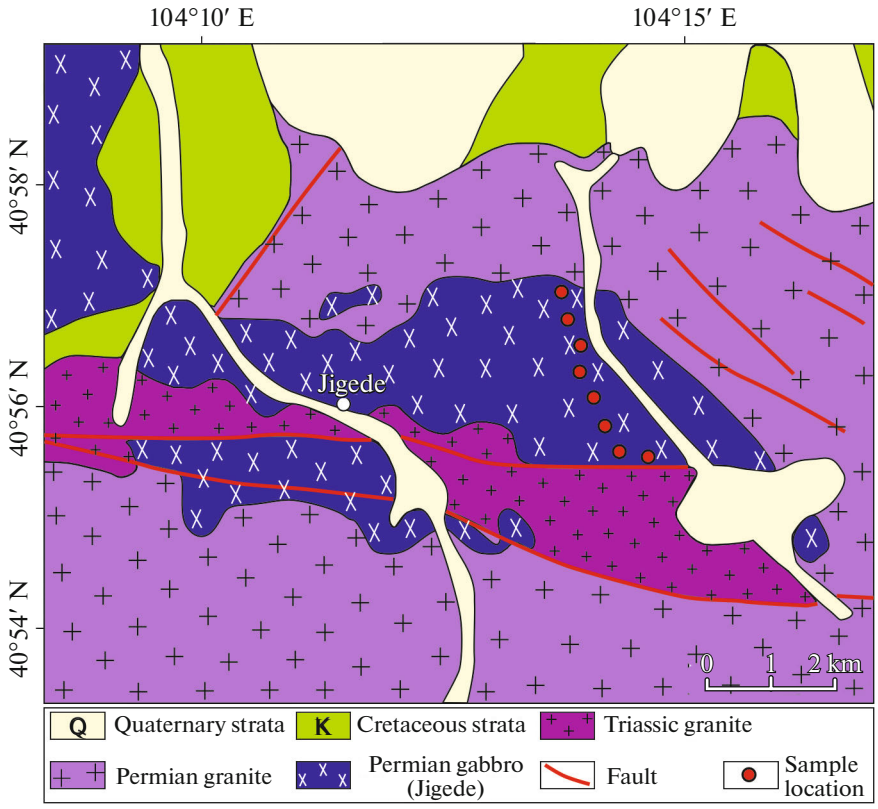

Fig. 2. Geological map of the Jigede intrusion. The sampling locations are also shown.

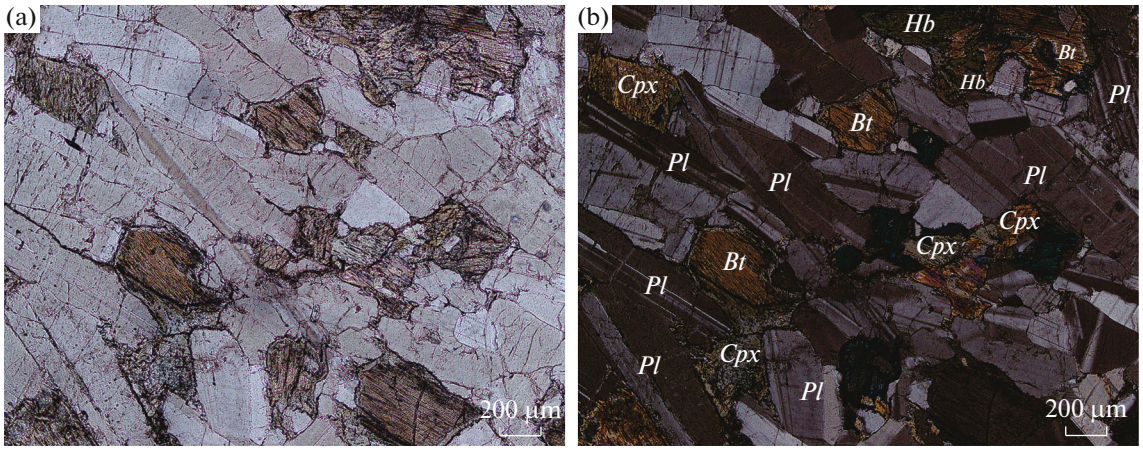

Fig. 3. Representative photomicrographs of the Jigede gabbro. *Bt*—biotite, *Cpx*—clinopyxene, *Hb*—hornblende, *Pl*—plagioclase.

(Fig. 2). The samples collected from the intrusion are medium to fine-grained gabbros, which consisted of plagioclase (60–70%), clinopyxene (~10–20%), biotite (~10–15%), and amphibole (~5%) (Fig. 3). We collect eight representative samples from the Jigede intrusion for whole-rock geochemical and Sr-Nd isotopic analysis. Sample 16CG-20 was collected for zircon separation and U-Pb dating. The detailed sampling locations are illustrated in Fig. 2.

ANALYTICAL METHODS

Zircon LA-ICP-MS U-Pb Dating

We separated zircons from the Sample 16CG-20 through conventional heavy liquid and magnetic separation methods, and then handpicked them with a binocular microscope. Representative zircon crystals were prepared and placed on a glass slide and covered with epoxy resin in a cylindrical frame. The surface of

this side was polished for further cathodoluminescence (CL) investigations. CL images were obtained using a GATAN MINI probe placed on the JSM 6510 electron microprobe, with an accelerating potential of 10 kV at Beijing GeoAnalysis Co. Ltd., China. LA-ICP-MS U-Pb analyses for these zircons were conducted at the State Key Laboratory for Mineral Deposits Research, Nanjing University (SKLMDR, NJU), determined by an Agilent 7500a ICP-MS equipped with a New Wave Research 213 nm laser ablation system. Analytical procedures are described by Xu et al. (2009) and Jackson et al. (2004) in detail. We corrected mass discrimination of the mass spectrometer and residual elemental fractionation through calibration against a homogeneous standard zircon, GEMOC/GJ-1 (608.53 ± 0.37 Ma, $n = 8$, 2σ; Jackson et al., 2004). The standard zircon Mud Tank (TIMS = 732 ± 5 Ma, $n = 5$, Black, Gulson, 1978; LA-ICP-MS $^{206}Pb/^{238}U$ = 732.4 ± 1.4 Ma, n = 359 at 95% confidence, Jackson et al., 2004) was determined as an independent control on reproducibility and instrument stability. We evaluated common Pb contents and corrected common Pb following a method introduced by Andersen (2002).

Major and Trace Elements, and Whole-rock Sr-Nd Isotope Analysis

Major element contents were analyzed using XRF on fused glass beads at SKLMDR, NJU, with precision better than 5%. When it comes to analyzing trace elements, for each sample, about 50 mg of powder was dissolved in s screw-top Teflon beaker, mixed with HF/HNO_3 mixture acid, and then heated at about 160°C for 48 h. We determined whole-rock trace element contents through a Finnigan Element II inductively coupled plasma mass spectrometry (ICP-MS) at the State Key Laboratory of Continental Dynamics, Northwest University (SKLCD, NWU), with precision better than 10%. Detailed methods for trace elements analyses are presented in (Gao et al., 2003).

The Sr-Nd isotopic ratios were measured using a Finnigan Triton TI thermal ionization mass spectrometer (TIMS) at SKLMDR, NJU. For Sr-Nd isotopic analyses, about 100 mg of powder was dissolved in Teflon beakers with a HF + HNO_3 mixture acid, and Sr and Nd were then separated and purified by conventional cation-exchange technique. Detailed analytical procedures are elaborated by (Pu et al., 2004, 2005). The mass fractionation corrections about $^{87}Sr/^{86}Sr$ and $^{143}Nd/^{144}Nd$ ratios are on the basis of $^{86}Sr/^{88}Sr$ of 0.1194 and $^{146}Nd/^{144}Nd$ of 0.7219, respectively. During the analyses, measurements for the La Jolla standard gave $^{143}Nd/^{144}Nd$ of 0.511842 ± 4 (2σ, $n = 5$), and for NBS-987 Sr standard gave $^{87}Sr/^{86}Sr$ of 0.710260 ± 10 (2σ, $n = 30$). Total analytical blanks were 5×10^{-11} g for Sm-Nd and $(2–5) \times 10^{-10}$ g for Rb-Sr.

RESULTS

LA-ICP-MS zircon U-Pb Dating

The zircons separated from 16CG-20 ranged from 50 to 100 μm in length and exhibited no oscillatory zoning (Fig. 4). They have high Th/U ratios in the range of 0.20 and 0.71 (Table 1), indicating magmatic origins (Williams et al., 1996; He et al., 2018). All U-Pb data that we obtained clustered on the concordant curves (Fig. 4) and produced a weighted mean $^{206}Pb/^{238}U$ age of 262 ± 4 Ma (1σ, MSWD = 1.4) for 16CG-20 (Fig. 4), suggesting that the Jigede intrusion was emplaced during the middle Permian.

Bulk Geochemistry and Sr-Nd Isotope

The Jigede intrusion has a low SiO_2 content of 49.80 to 52.22 wt % (Table 2; Fig. 5). Compared to the experimental partial melts of mantle rocks, all the samples contain similar abundance of MgO (11.15–12.15 wt %), low contents of TiO_2 (0.24–0.37 wt %) and $Fe_2O_3^T$ (4.87–5.41 wt %), as well as high levels of CaO (11.45–12.75 wt %), Al_2O_3 (14.18–17.08 wt %) and Mg# (0.81–0.83) (Table 2, Fig. 6). Meanwhile, the samples are enriched in LREEs relative to HREEs, with positive Eu anomalies (Fig. 7a). In PM-normalized spidergrams, all samples exhibit notably negative Th, Nb, Zr-Hf, Ti anomalies as well as positive U and Sr anomalies (Fig. 7b). Compared to mid-ocean-ridge basalt (MORB), the Jigede gabbros are depleted in REEs and HFSEs, but enriched in LILEs (Fig. 7b). These mafic samples have low initial $^{87}Sr/^{86}Sr$ in the range of 0.7046 to 0.7054, and positive $\varepsilon_{Nd}(T)$ values of + 1.8 and + 4.8 (Table 3).

DISCUSSION

Crustal Assimilation

The Jigede intrusion contains basaltic components with low SiO_2 abundances of 49.80–52.22 wt % (Table 2). During the emplacement of the basaltic magma, continental components may contaminate and modify the initial melt. In this regard, the ratios of isotopes and strongly incompatible elements can serve as indicators of crustal contamination as they are not disturbed by pure fractional crystallization. Continental crust, especially upper crust, is relatively enriched in La, but depleted in Nb, with a low Nb/La ratio (0.39) (Rudnick, Gao, 2003). However, the Jigede gabbros exhibit lower Nb/La ratios (0.13 to 0.19) than upper continental crust (Fig. 8a), implying that the depletion of Nb is not associated with crustal contamination. Furthermore, the Nb/La ratios of all samples were found to be relatively constant and showed no apparent correlation with their SiO_2 levels (Fig. 8a). The low initial Sr isotopic ratios, positive $\varepsilon_{Nd}(T)$ values as well as the slightly positive correlation between $\varepsilon_{Nd}(T)$ and SiO_2 also suggested that the contamination, if any, is relatively minor (Fig. 8b). Most importantly, significant crustal contamination is not reconcilable with the

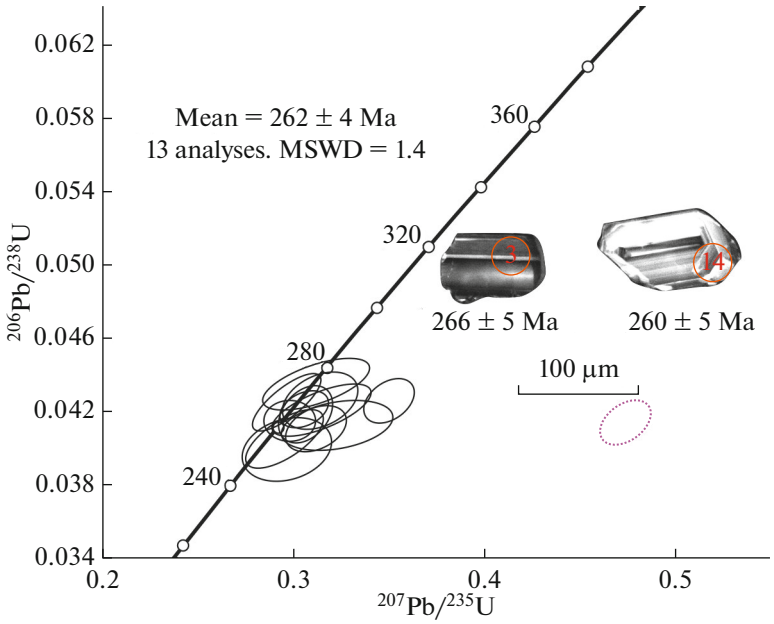

Fig. 4. LA-ICP-MS zircon U-Pb concordant curves and typical CL images of representative zircons collected from the sample 16CG-20.

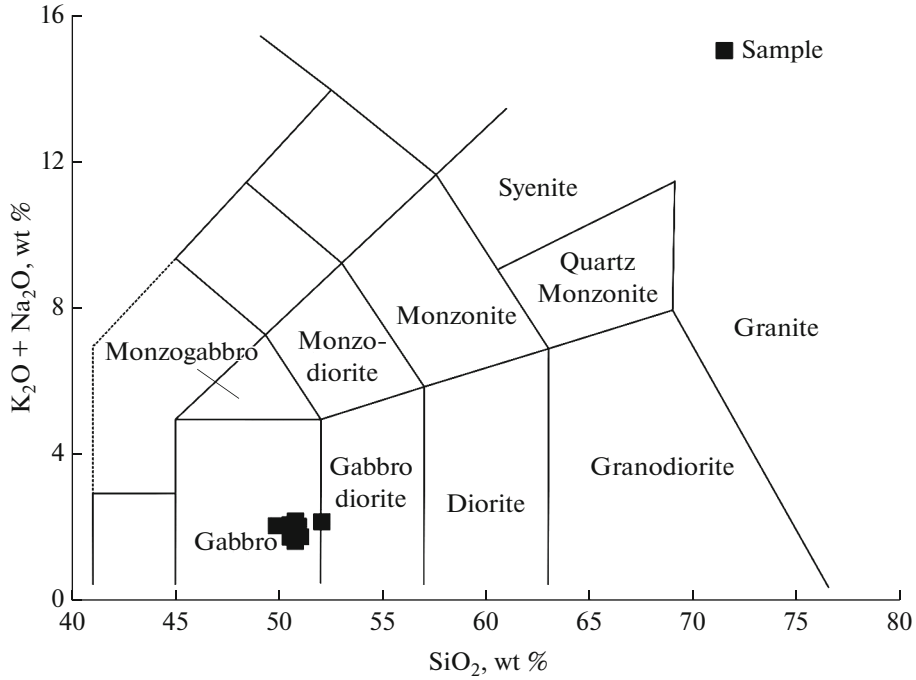

Fig. 5. TAS-diagram (Le Maitre, 2002) of the Jigede intrusion.

markedly negative Zr-Hf anomalies in the spider diagrams (Fig. 7b).

Mineral Cumulation

Figure 3 shows a partly-densified, texturally equilibrated mosaic of plagioclase. The petrographic feature provided clear evidence of plagioclase accumulation in the Jigede intrusion (Hunter, 1996; Fig. 3). This is further supported by the positive Sr and Eu anomalies in the REE and trace element patterns (Fig. 7). Compared to those experimental partial melts of mantle rocks, the Jigede gabbros have high CaO and Al_2O_3 contents (Fig. 6c), which also entailed the cumulation

Table 1. LA-ICP-MS U-Pb isotopic analysis for zircons from the Jigede gabbro (sample 16CG-20)

Spot	Th, ppm	U, ppm	Th/U	$^{207}Pb/^{206}Pb$	1σ	$^{207}Pb/^{235}U$	1σ	$^{206}Pb/^{238}U$	1σ	$^{208}Pb/^{232}Th$	1σ	$^{07}Pb/^{206}Pb$	1σ	$^{207}Pb/^{235}U$	1σ	$^{206}Pb/^{238}U$	1σ
1	140	230	0.61	0.0529	0.0020	0.2935	0.0101	0.0400	0.0007	0.0113	0.0003	323	93	260	8	252	5
2	172	280	0.61	0.0550	0.0024	0.3105	0.0110	0.0407	0.0007	0.0139	0.0003	407	93	273	7	255	5
3	38	190	0.20	0.0571	0.0023	0.3264	0.0103	0.0412	0.0008	0.0131	0.0004	446	90	277	8	266	5
4	90	176	0.51	0.0517	0.0031	0.3102	0.0174	0.0432	0.0007	0.0129	0.0004	277	98	272	11	274	6
5	674	1408	0.49	0.0840	0.0028	0.4812	0.0099	0.0416	0.0007	0.0189	0.0003	1289	62	399	7	263	4
6	30	123	0.24	0.0562	0.0041	0.3170	0.0211	0.0420	0.0006	0.0144	0.0007	445	137	271	11	261	6
7	110	340	0.32	0.0510	0.0020	0.3023	0.0090	0.0427	0.0008	0.0127	0.0006	283	78	268	4	270	5
8	130	215	0.60	0.0520	0.0024	0.3035	0.0120	0.0420	0.0009	0.0132	0.0004	285	103	268	8	266	6
9	100	140	0.71	0.0530	0.0029	0.3031	0.0127	0.0413	0.0008	0.0130	0.0004	309	97	268	7	263	5
10	82	170	0.48	0.0545	0.0022	0.3239	0.0112	0.0424	0.0006	0.0132	0.0004	420	93	280	7	269	5
11	153	612	0.24	0.0533	0.0019	0.3174	0.0082	0.0426	0.0008	0.0140	0.0003	348	72	279	6	271	5
12	206	704	0.30	0.0535	0.0019	0.3010	0.0071	0.0419	0.0007	0.0138	0.0002	323	72	264	5	259	4
13	55	210	0.26	0.0525	0.0025	0.3087	0.0133	0.0421	0.0008	0.0140	0.0007	321	110	271	8	266	5
14	114	322	0.33	0.0529	0.0019	0.2992	0.0087	0.0409	0.0007	0.0129	0.0003	325	86	264	7	260	5

Table 2. Whole-rock major element oxides (wt %), trace elements (ppm) and REE (ppm) abundances of selected rocks samples

Sample	16CG-13	16CG-14	16CG-15	16CG-16	16CG-17	16CG-18	16CG-19	16CG-20
SiO_2	50.71	50.82	50.42	50.54	49.80	50.91	52.22	50.43
TiO_2	0.27	0.28	0.26	0.26	0.24	0.27	0.37	0.26
Al_2O_3	16.18	16.48	17.08	16.20	17.08	15.46	14.18	16.16
$^{T}Fe_2O_3$	5.15	5.41	4.87	5.25	4.87	5.07	5.39	5.12
MnO	0.11	0.11	0.10	0.11	0.10	0.11	0.12	0.11
MgO	12.05	11.35	11.15	12.05	11.15	12.05	12.15	11.75
CaO	11.60	12.75	11.70	12.10	11.90	12.40	11.95	11.45
Na_2O	1.62	1.88	1.84	1.64	1.80	1.62	1.92	1.56
K_2O	0.19	0.09	0.15	0.15	0.17	0.16	0.18	0.20
P_2O_5	0.02	0.01	0.01	0.02	0.02	0.01	0.02	0.02
LOI	2.10	0.55	1.94	1.18	2.21	1.65	1.25	2.27
Total	100.00	99.73	99.52	99.50	99.34	99.71	99.75	99.33
Mg#	0.82	0.81	0.82	0.82	0.82	0.83	0.82	0.82
Ba	20	30	30	40	50	20	60	20
Rb	8.5	4	5.7	6.8	7.2	7.2	8.1	8.5
Sr	330	393	347	318	368	365	305	329
Y	5.7	6.3	5.4	5.5	5.1	6	7.5	5.4
Zr	10	6.6	6.9	7.3	7.1	7.8	9.8	9.6
Nb	0.3	0.2	0.2	0.2	0.2	0.2	0.2	0.2
Th	0.29	0.27	0.21	0.24	0.23	0.16	0.26	0.28
Pb	1.3	1.4	1.2	1.6	1.4	1.4	1.3	1.5
Ga	12.05	12.1	12.5	11.9	12.35	11.35	10.75	11.75
Ni	225	329	237	252	284	206	178.5	243
V	96	108	96	97	91	105	126	96
Cr	360	491	378	419	454	558	344	387
Hf	0.3	0.3	0.3	0.3	0.3	0.3	0.4	0.3
Ta	<0.05	<0.05	<0.05	<0.05	<0.05	<0.05	<0.05	<0.05
U	1	0.2	0.4	0.5	0.6	0.1	0.2	1.1
La	1.6	1.5	1.5	1.5	1.5	1.4	1.5	1.5
Ce	3.85	3.88	3.76	3.88	3.78	3.37	4.11	3.87
Pr	0.57	0.55	0.54	0.55	0.54	0.51	0.64	0.59
Nd	2.8	2.8	2.7	2.7	2.7	2.6	3.4	2.6
Sm	0.85	0.81	0.82	0.82	0.72	0.88	1.07	0.85
Eu	0.37	0.41	0.38	0.39	0.37	0.37	0.46	0.39
Gd	0.94	1.11	0.96	0.97	0.87	0.99	1.29	1.01
Tb	0.16	0.17	0.15	0.15	0.14	0.16	0.2	0.15
Dy	0.99	1.05	0.97	0.99	0.88	1.12	1.32	0.94
Ho	0.2	0.23	0.21	0.21	0.19	0.23	0.28	0.2
Er	0.61	0.67	0.57	0.58	0.56	0.66	0.82	0.59
Tm	0.09	0.1	0.08	0.09	0.08	0.1	0.12	0.09
Yb	0.54	0.61	0.54	0.53	0.52	0.57	0.71	0.54
Lu	0.08	0.09	0.08	0.08	0.08	0.09	0.11	0.08

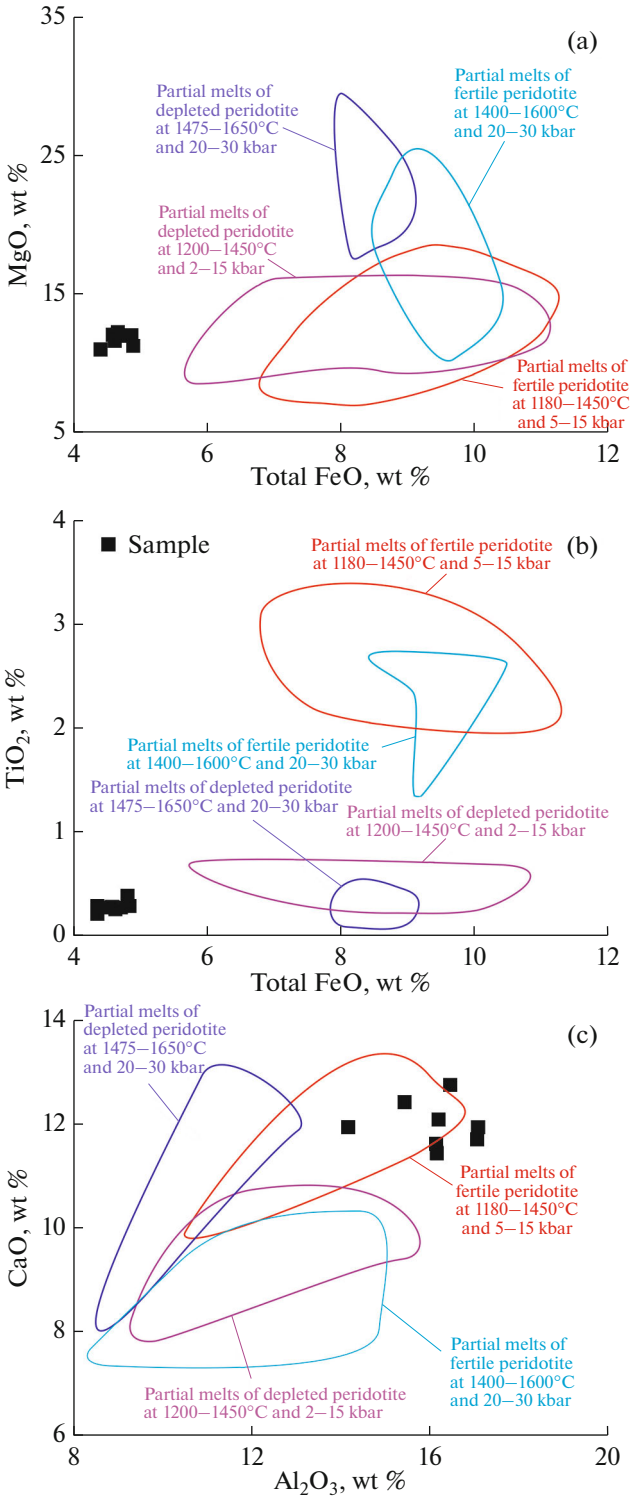

Fig. 6. Plots of (a) MgO vs. Total FeO, (b) TiO_2 vs. total FeO and (c) CaO vs. Al_2O_3 for the Jigede intrusion. The fields of some experimental melts of depleted and fertile peridotites are also exhibited (Falloon et al, 1988).

of plagioclase. Relative to MORB, the low abundances of REEs and HFSEs abundances in the Jigede gabbros can be also attributed to plagioclase cumulation due to their strongly incompatibility in the mineral (Fig. 7). In the thin section, we did not observe any significant accumulation of mafic minerals (Fig. 3). The positive correlation between $Fe_2O_3^T$, MgO, TiO_2 and SiO_2 further precluded the cumulation of mafic minerals and Ti-Fe oxides (Fig. 9).

Source Nature

Strongly incompatible element ratios and Sr-Nd isotopic components are not generally disturbed by fractional crystallization or cumulation of minerals. Thus, they can be used to infer source nature. Relative to HREEs, all the samples are evidently enriched in LREEs ($(La/Yb)_n$ = 1.52–2.13) (Fig. 7a) and exhibit significantly different $(^{87}Sr/^{86}Sr)_i$ (0.7046 to 0.7054) and $\varepsilon_{Nd}(T)$ (+ 1.8 to + 4.6) from MORB (Table 3). Thus, the Jigede intrusion might originate from a modified subcontinental lithospheric mantle or an ocean-island-basalt (OIB)-like mantle rather than a MORB-like mantle source. On the other hand, the low contents of incompatible elements and the depletion of Nb, Zr-Hf as well as Ti in the PM-normalized spidergrams argue against an OIB-like mantle source (Fig. 7b; Sun and McDonough, 1989). Experimental studies revealed that the partial melts of fertile peridotite have higher TiO_2 contents (>1 wt %) than those (<1 wt %) derived from depleted peridotite at a given FeO^T content (Fig. 6b). The Jigede intrusion exhibits a low TiO_2 level in the range of 0.24–0.37 wt %, indicating a depleted mantle source. The greatest possibility is a lithospheric mantle source. The relative depletion of these HFSEs has been interpreted as an indicator of a subduction process (Thirlwall et al., 1994). Taken together, we tentatively conclude that the Jigede intrusion was most likely to have originated from a subcontinental lithospheric mantle source modified by subducted slab-derived components (fluids or melts). Furthermore, both HFSEs and REEs (e.g., Th, Y, Zr, Hf, Ti and Nb) are more immobile in fluids than in melts (Kepezhinskas et al., 1997; Zhao and Zhou, 2007). Thus, relative to LILEs, the depletion of Th, Zr-Hf and Ti in the trace element patterns indicates the introduction of slab fluids into the overlying mantle source (Fig. 7b; Liu et al., 2018). The positive U anomaly and high Th/U ratio can be attributed to preferential partitioning of U into aqueous fluid coexisting with subducted eclogitic slab (Brenan et al., 1995a, 1995b). The fluid involvement is also supported by the presence of hornblende (water-bearing mineral) in the mineral assemblages. REEs ratios can be used to explore the formation depths of basaltic magmas (McKenzie and O'Nions, 1991). The low $(Dy/Yb)_n$ ratios (1.13 to 1.32) coupled with flat HREE pattens (Fig. 7a) indicated that the formation of the

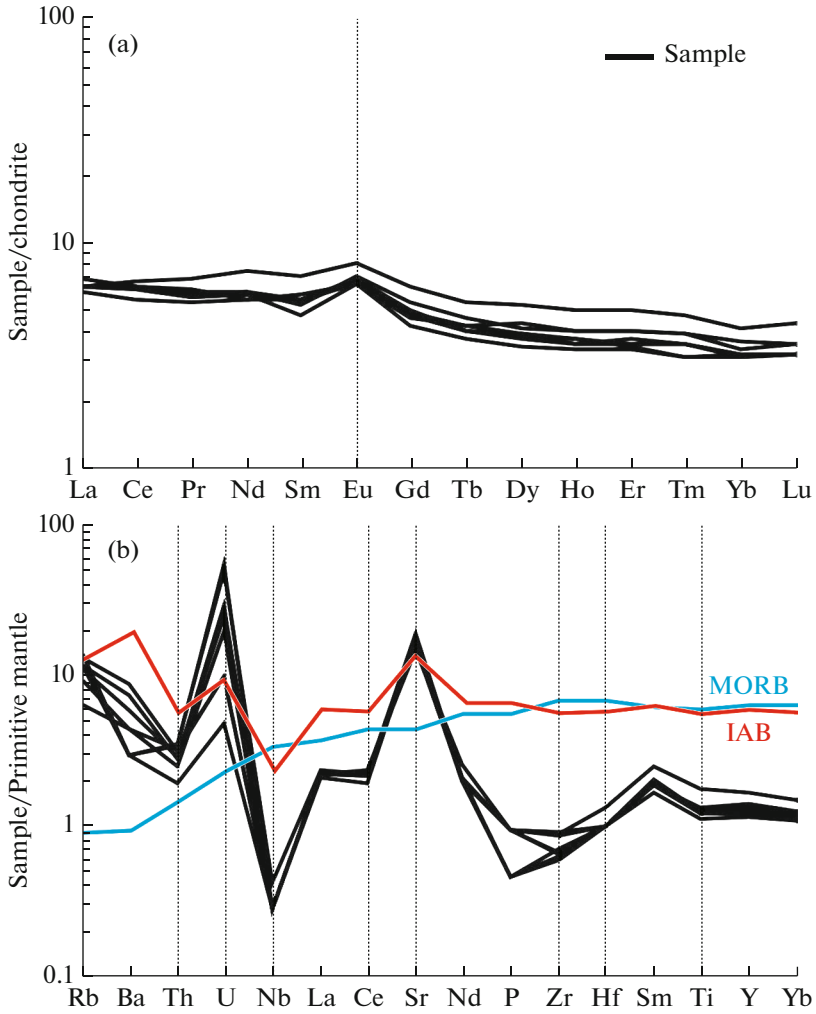

Fig. 7. (a) Chondrite-normalized (Sun, McDonough, 1989) REE patterns and (b) primitive mantle-normalized (Sun, McDonough, 1989) trace element patterns for the Jigede intrusion.

initial melts came from the spinel stability field (Liao et al., 2015; Liu et al., 2015). Thus, melting depth is not more than 80 km (Robinson and Wood, 1998). Such a shallow depth is reconciled with the lithospheric source. In sum, the Jigede intrusion was likely derived from partial melting of a shallow lithospheric mantle source that had been modified by slab-released fluids, with subsequent cumulation of plagioclase.

Table 3. Sr-Nd isotopic components of the studied intrusions

Sample	16CG-13	16CG-14	16CG-15	16CG-16	16CG-17	16CG-18	16CG-19	16CG-20
$^{87}Rb/^{86}Sr$	0.0745	0.0294	0.0475	0.0619	0.0566	0.0571	0.0768	0.0747
$^{87}Sr/^{86}Sr$	0.705345	0.705545	0.705155	0.705211	0.705180	0.705420	0.704883	0.705285
$\pm 2\sigma$	0.000004	0.000004	0.000004	0.000003	0.000004	0.000004	0.000003	0.000004
$(^{87}Sr/^{86}Sr)_i$	0.7051	0.7054	0.7050	0.7050	0.7050	0.7052	0.7046	0.7050
$^{147}Sm/^{144}Nd$	0.1834	0.1748	0.1835	0.1835	0.1611	0.2045	0.1901	0.1975
$^{143}Nd/^{144}Nd$	0.512749	0.512741	0.512707	0.512744	0.512776	0.512788	0.512864	0.512762
$\pm 2\sigma$	0.000004	0.000003	0.000004	0.000003	0.000004	0.000005	0.000007	0.000005
$\varepsilon_{Nd}(T)$	2.6	2.8	1.8	2.5	3.9	2.7	4.6	2.4

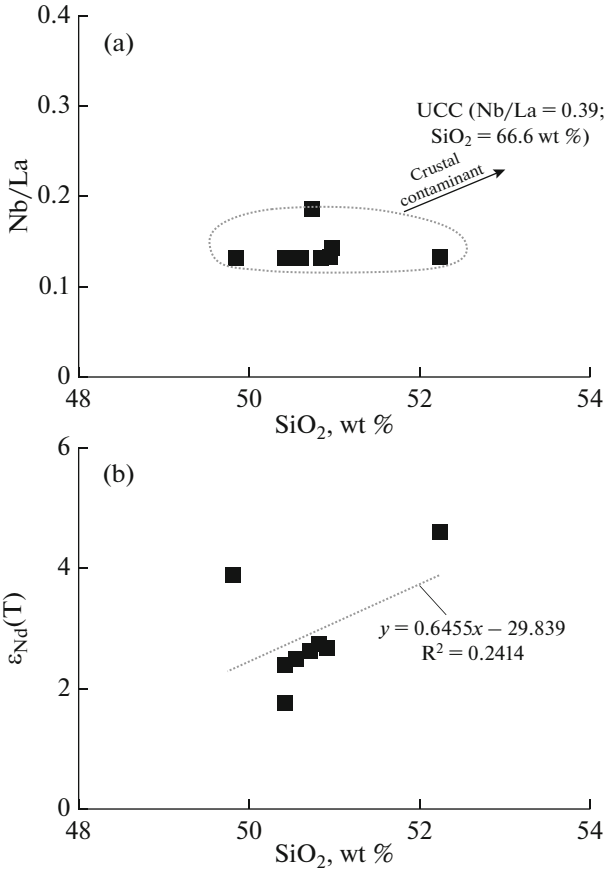

Fig. 8. Plots of (a) Nb/La, (b) $\varepsilon_{Nd}(T)$ and SiO_2 for the Jigede intrusion. UCC: upper continental crust. The data of UCC are from Rudnick and Gao (2003).

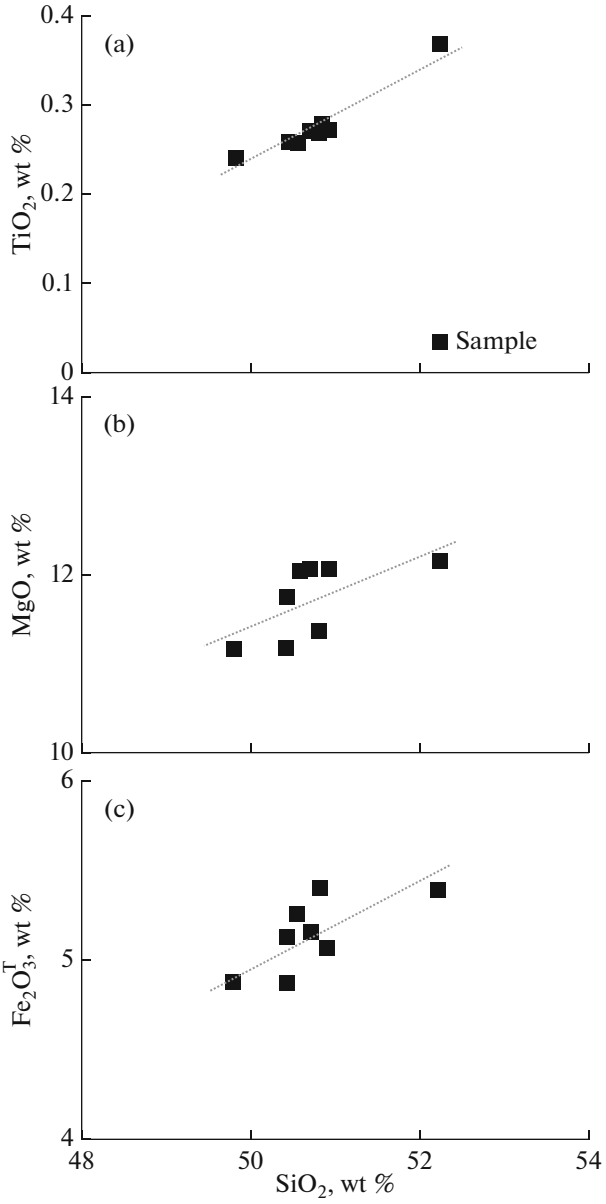

Fig. 9. Plots of SiO_2 vs. (a) TiO_2, (b) MgO and (c) $Fe_2O_3^T$ for the Jigede intrusion.

Tectonic Implications

Previous studies have identified a giant flare-up of Permian magmatic rocks in the Alxa Block (Shi et al., 2012; Zhang et al., 2013; Dan et al., 2014; Lin et al., 2014, 2017a, 2017b). The predominance of granitoids (ca. 280 Ma) has been considered to be reconciled with a silicic igneous province. Dan et al. (2014) further proposed that the Alxa silicic igneous province was produced by the ca. 280 Ma Tarim mantle plume activities. Indeed, the Alxa silicic igneous province is smaller (ca. 0.05 Mkm^2) than other typical silicic igneous provinces, which generally cover an area extent of > 0.10 Mkm^2 (Bryan, 2007). More importantly, high-*T* continental flood basalts, komatiitic sequences, and mafic intrusions are not absent in the Alxa Block. Thus, the occurrence of Permian magmatic rocks cannot be attributed to mantle plume activities. Shi et al. (2014) advocated that the Permian magmatic rocks were emplaced in a post-collisional setting. Several Middle to Late Permian (266 to 250 Ma) intrusions (Baogeqi, Hurentaolegai, Wuliji and Sharijimiao) from the Shalazhashan belt are bimodal rock associations with high-K calc-alkaline affinities, considered to have been emplaced in post-collisional settings (Shi et al., 2014). However, bimodal magmatic suites are not restricted to the post-collision setting. It is also plausible for the emplacement of bimodal magmatic suites in a back-arc basin or hinterland of an active continental margin above the subducted slab (Liu et al., 2015). Recently, on the basis of whole-rock Nd and in-situ zircon Hf isotopic data on magmatic rocks, a significant variation occurring at between 280 and 265 Ma has been identified (Liu et al., 2017a, 2017b). The authors proposed that the sudden change in the Nd-Hf isotopic ratios was in response to a tectonic switch from an oceanic subduction setting to a post-

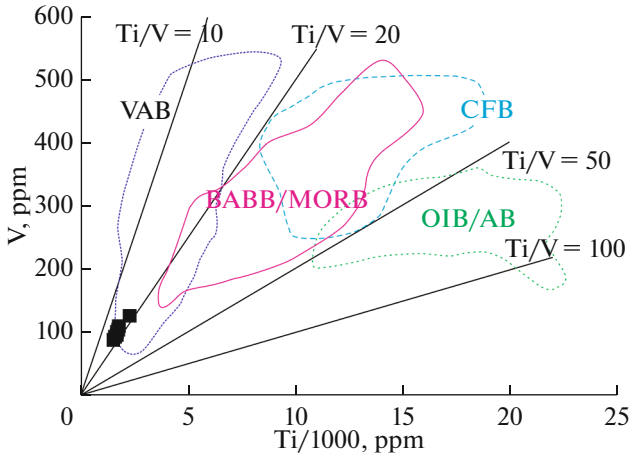

Fig. 10. V vs. Ti/1000 tectonic discriminant diagram (Shervais, 1982) for the Jigede intrusion. Also shown are the fields for volcanic arc basalts (VAB), mid-ocean-ridge basalt (MORB)/back-arc basin basalts (BABB), continental flood basalts (CFB), and ocean-island basalts (OIB)/alkali basalts (AB) (Rollinson, 1993).

collisional setting. In addition, slab roll-back can also lead to the isotopic change (Sun et al., 2017).

The Jigede intrusion is characterized by HFSEs depletions and negative Th-Nb-Ti anomalies, which are inconsistent with the geochemical features of a plume-related OIB (Fig. 7b). Instead, its petrogenesis revealed that its lithospheric mantle source had been strongly modified by slab-derived fluids. All the samples exhibited arc geochemical signatures, indicative of an oceanic subduction setting. They exhibit relatively low Ti/V ratios (< 20) that can be reconciled with volcanic arc basalts (Fig. 10). We thus argue that the emplacement of the Permian magmatic rocks was more likely to have occurred in subduction setting. This is also supported by the following evidence. First, SHRIMP zircon U-Pb dating of the gabbros from the Quagan Qulu ophiolite yielded a weighed mean age of 275 ± 3 Ma (Zheng et al., 2014). They are significantly enriched in LILEs relative to HFSEs and LREEs, which suggests that they were emplaced in a back-arc basin. Furthermore, dating of deformed porphyries from the Langshan area resulted in emplacement ages of 291.7 to 284.7 Ma (Lin et al., 2014). The deformation was likely associated with subduction-induced compression. The timing of the final closure should be later than the Early Permian. Second, the Late Carboniferous to Middle Permian Bijiertai, Hongqueryulin, and Qinggele mafic-ulramafic rocks (306 to 262 Ma) display evident arc geochemical characteristics, implying that the Paleo-Asian oceanic subduction has continued to the Middle Permian (Feng et al., 2013). Third, the Late Paleozoic sedimentary sequence and paleontological assemblages on the northern and southern sides of the Enger Us ophiolite belt are obviously different (Wang et al., 1994). And there is Late Triassic continental molasse exposed in the Alxa Block (Wang et al., 1994), indicating the final closure of the Paleo-Asian Ocean occurred during Late Permian to Late Triassic. To sum up, the Permian magmatic rocks were emplaced in a subduction setting, and the final closure of the Paleo-Asian Ocean did not occur prior to the Middle Permian.

CONCLUSIONS

(1) The Jigede intrusion from the Shalazhanshan belt was emplaced in the Middle Permian (~262 Ma).

(2) The Jigede intrusion is gabbro and exhibits arc geochemical characteristics. It was likely to have resulted from partial melting of a shallow lithospheric mantle source modified by slab-released fluids, with subsequent cumulation of plagioclase.

(3) The emplacement of the Jigede intrusion was in response to the Paleo-Asian oceanic subduction.

(4) The final closure of the Paleo-Asian ocean did not occur prior to the Middle Permian.

FUNDING

This study is financially supported by the National Natural Science Foundation of China (grants 41703022), Fundamental Research Funds for the Central Universities (lzujbky-2018-52), Plateau mountain ecology and Earth's environment discipline construction project (grants C176240107), Joint Foundation Project between Yunnan Science and Technology Department and Yunnan University (grants C176240210019), and Geology Discipline Construction Project of Yunnan University (C176210227).

REFERENCES

Andersen, T., Correction of common lead in U-Pb analyses that do not report ^{204}Pb, *Chem. Geol.,* 2002, vol. 192, pp. 59–79.

Brenan, J.M., Shaw, H.F., Ryerson, F.J., and Phinney, D.L., Mineral-aqueous fluid partitioning of trace elements at 900°C and 2.0 GPa: constraints on the trace element chemistry of mantle and deep crystal fluids, *Geochim Cosmochim Acta,* 1995a, vol. 59, pp. 3331–3350.

Brenan, J.M., Shaw, H.F., and Ryerson, F.J., Experimental evidence for the origin of lead enrichment in convergent margin magmas, *Nature,* 1995b, vol. 378, pp. 54–56.

Black,L.P. dand Gulson, B.L., The age of the Mud Tank carbonatite, Strangways Range, Northern Territory, *BMR, J. Austral. Geol. Geophys.,* 1978, vol. 3, pp. 227–232.

Bryan, S., Silicic large igneous provinces, *Episodes,* 2007, vol. 30, pp. 20–31.

Dan, W., Li, X.H., Wang, Q., Tang, G.J., and Liu, Y., An Early Permian (ca. 280 Ma) silicic igneous province in the Alxa Block, NW China: a magmatic flare-up triggered by a mantle-plume?, *Lithos,* 2014a, vol. 204, pp. 144–158.

Falloon, T.J., Green, D.H., Hatton, C.J., and Harris, K.L., Anhydrous partial melting of a fertile and depleted peridotite from 2 to 30 kb and application to basalt petrogenesis, *J. Petrol.,* 1988, vol. 29, pp. 1257–1282.

Feng, J.Y., Xiao, W.J., Windley, B., Han, C.M., Wan, B., Zhang, J.E., Ao, S.J., Zhang, Z.Y., and Lin, L.N., Field geology, geochronology and geochemistry of mafic–ultramafic rocks from Alxa, China: implications for Late Permian accretionary tectonics in the southern Altaids, *J. Asian Earth Sci.,* 2013, vol. 78, pp. 114–142.

Gao, J.F., Lu, J.J., Lai, M.Y., Lin, Y.P., and Pu, W., Analysis of trace elements in rock samples using HR-ICPMS, *J. Nanjing Univ. (Natural Sciences),* 2003, vol. 39, pp. 844–850 (in Chinese with English abstract).

Han, B.F., He, G.Q., Wang, X.C., and Guo, Z.J., "Late Carboniferous collision between the Tarim and Kazakhstan-Yili terranes in the western segment of the South Tian Shan Orogen, Central Asia, and implications for the Northern Xinjiang, western China," *Earth Sci. Rev.,* 2011, vol. 109, pp. 74–93.

He, X.H., Zhong, H., Zhao, Z.F., Tan, S.C., Zhu, W.G., Yang, S.Q., Hu, W.J., Tang, Z., and Bao, C.F., U-Pb geochronology, elemental and Sr-Nd isotopic geochemistry of the Houyaoyu granite porphyries: implications for the genesis of Early Cretaceous felsic intrusions in East Qinling, *J. Earth Sci.,* 2018, vol. 29, pp. 920–938.

Hunter, R.H., *Texture development in cumulate rocks, Layered Intrusions,* Cawthorn, R.G., Ed., Amsterdam: Elsevier, 1996, pp. 77–101.

Jahn, B.-M., The Central Asian Orogenic Belt and growth of the continental crust in the Phanerozoic, *Geol. Soc., London, Spec. Publ.,* 2004, vol. 226, pp. 73–100

Jackson, S.E., Pearson, N.J., Griffin, W.L., and Belousova, E.A., The application of laser ablation-inductively coupled plasma-mass spectrometry to in situ U-Pb zircon geochronology, *Chem. Geol.,* 2004, vol. 211, pp. 47–69.

Kepezhinskas, P., McDermott, F., Defant, M., Hochstaedter, A., Drummond, M.S., Hawdesworth, C.J., Koloskov, A., Maury, R.C., Bellon, H., Trace element and Sr-Nd-Pb isotopic constraints on a three-component model of Kamchatka Arc petrogenesis. *Geochim. Cosmochim. Acta,* 1997, vol. 61, pp. 577–600.

Khain, E.V., Bibikova, E.V., Salnikova, E.B., Kröner, A., Gibsher, A.S., Didenko, A.N., Degtyarev, K.E., and Fedotova, A.A., The Palaeo-Asian ocean in the Neoproterozoic and early Palaeozoic: new geochronologic data and palaeotectonic reconstructions, *Precambrian Res.,* 2003, vol. 122, pp. 329–358.

Kovach, V.P., Matukov, D.I., Berezhnaya, N.G., Kotov, A.B., Levitsky, V.I., Barash, I.G., Kozakov, I.K., Levsky, L.K., and Sergeev, S.A., SHRIMP zircon age of the Gargan block tonalites – find Early Precambrian basement of the Tuvino-Mongolian microcontinent, *Central Asia mobile belt 32th Intern. Geological Congress,* Florence: 2004, Pt 2, no. 1263.

Kozakov, I.K., Stuctural features and metamorphism of the Precambrian granitoids of the Sangilen highland, Tuva, *Geol. Geofiz.,* 1976, no. 12, pp. 159–160.

Kozakov, I.K. and Azimov, P.Ya., Geodynamics of the origin of granulites in the Sangilen Block of the Tuva–Mongolian Terrane, Central Asian Orogenic Belt, *Petrology,* 2017, vol. 25, no. 6, pp. 615–624.

Kozakov, I.K., Kotov, A.B., Salnikova, E.B., et al., Metamorphic age of crystalline complexes of the Tuva–Mongolia massif: the U–Pb geochronology of granitoids, *Petrology,* 1999, vol. 7, no. 2, pp. 177–191.

Kröner, A., Kovach, V., Belousova, E., Hegner, E., Armstrong, R., Dolgopolova, A., Seltmann, R., Alexeiev, D.V., Hoffmann, J.E., Wong, J., Sun, M., Cai, K., Wang, T., Tong, Y., Wilde, S.A., Degtyarev, K.E., and Rytsk, E., Reassessment of continental growth during the accretionary history of the Central Asian Orogenic Belt, *Gondwana Res.,* 2014, vol. 25, pp. 103–125.

Kröner, A., Kovach, V., Alexeiev, D., Wang, K.L., Wong, J., Degtyarev, K., and Kozakov, I., 2017. No excessive crustal growth in the Central Asian Orogenic Belt: Further evidence from field relationships and isotopic data, *Gondwana Res.,* 2017.
http://dx.doi.org/10.1016/j.gr.2017.04.006

Le Maitre, R.W., *Igneous Rocks: A Classification and Glossary of Terms*, 2nd. Ed, Cambridge: Cambridge University Press, 2002.

Liao, S.Y., Wang, D.B., Tang, Y., Yin, F.G., Cao, S.N., Wang, L.Q., Wang, B.D., and Sun, Z.M., Late Paleozoic Woniusi basaltic province from Sibumasu terrane: Implications for the breakup of eastern Gondwana's northern margin, *Geol. Soc. Am. Bull.,* 2015.
https://doi.org/10.1130/B31210.1

Lin, L.N., Xiao, W.J., Wan, B., Windley, B.F., Ao, S.J., Han, C.M., Feng, J.Y., Zhang, J.E., and Zhang, Z.Y., Geochronology and geological evidence for persistence of south-dipping subduction to Late Permian time, Langshan area, Inner Mongolia (China): significance for termination of accretionary orogenesis in the southern Altaids, *Am. J. Sci.,* 2014, vol. 314, pp. 679–703.

Liu, Z., Zhou, Q., Lai, Y., Qing, C.S., Li, Y.X., Wu, J.Y., and Xia, X.B., Petrogenesis of the Early Cretaceous Laguila bimodal intrusive rocks from the Tethyan Himalaya: Implications for the break-up of Eastern Gondwana, *Lithos,* 2015, vol. 236–237, pp. 190–202.

Liu, Q., Zhao, G.C., Han, Y.G., Eizenhöfer, P.R., Zhu, Y.L., Hou, W.Z., and Zhang, X.R., Timing of the final closure of the Paleo-Asian Ocean in the Alxa Terrane: Constraints from geochronology and geochemistry of Late Carboniferous to Permian gabbros and diorites. *Lithos,* 2017a, vol. 274—275, pp. 19—30.

Liu, Q., Zhao, G.C., Han, Y.G., Eizenhöfer, P.R., Zhu, Y.L., Hou, W.Z., Zhang, X.R., and Wang, B., Geochronology and geochemistry of Permian to Early Triassic granitoids in the Alxa Terrane: constraints on the final closure of the Paleo-Asian Ocean, *Lithosphere,* 2017b.
https://doi.org/10.1130/L646.1

Liu, Z., Liao, S.Y., Zhou, Q., and Zhang, X., Petrogenesis of ore-bearing porphyry in non-subduction setting: a case study of the Eocene potassic intrusions in the western Yangtze Block, *Mineral. Petrol.,* 2018.
https://doi.org/10.1007/s00710-018-0597-4

Lu, J.C., Wei, X.Y., Li, Y.H., and Wei, J.S., Geochemical characteristics of CarboniferousPermian hydrocarbon source rocks of Xiangtan 9 well in Ejin Banner, western Inner Mongolia, *Geol. Bull. China,* 2012, vol. 31, no. 10, pp. 1628–1638 (in Chinese with English abstract).

McKenzie, D.A.N. and O'Nions, R.K., Partial melt distributions from inversion of rare earth element concentrations, *J. Petrol.,* 1991, vol. 32, pp. 1021–1091.

Pearce, J.A., Harris, N.B.W., and Tindle, A.G., Trace element discrimination diagrams for the tectonic interpretation of granitic rocks, *J. Petrol.,* 1984, vol. 25, pp. 956–983.

Pu, W., Zhao, K.D., Ling, H.F., and Jiang, S.Y., High precision Nd isotope measurement by Triton TI Mass Spectrometry, *Acta Geosci. Sinica,* 2004, vol. 25, pp. 271–274 (in Chinese with English abstract).

Pu, W., Gao, J.F., Zhao, K.D., Ling, H.F., Jiang, S.Y., Separation method of Rb–Sr, Sm–Nd using DCTA and HIBA, *J. Nanjing Univ. (Natural Sciences),* 2005, vol. 41, pp. 445–450 (in Chinese with English abstract).

Robinson, J.A.C. and Wood, B.J., The depth of the spinel to garnet transition at the peridotite solidus, *Earth Plane. Sci. Lett.,* 1998, vol. 164, pp. 277–284.

Rollinson, H.R., *Using Geochemical Data: Evaluation, Presentation, Interpretation,* London: Longman Publishing Group, 1993.

Rudnick, R.L. and Gao, S., Composition of the continental crust, *Treatise on Geochemistry, Volume 3,* Holland, H.D. and Turekian, K.K., Eds., Elsevier, 2003, p. 1–64.

Shervais, J.W., Ti–V plots and the petrogenesis of modern and ophiolitic lavas, *Earth Planet. Sci. Lett.,* 1982, vol. 59, pp. 101–118.

Şengör, A.M.C., Natal'in, B.A., and Burtman, V.S., Evolution of the Altaid tectonic collage and Palaeozoic crustal growth in Eurasia, *Nature,* 1993, vol. 364, pp. 299–307.

Shi, X.J., Tong, Y., Wang, T., Zhang, J.J., Zhang, Z.C., Zhang, L., Guo, L., Zeng, T., and Geng, J.Z., LA-ICP-MS zircon U-Pb age and geochemistry of the Early Permian Halinudeng granite in northern Alxa area, western Inner Mongolia, *Geol. Bull. China,* 2012, vol. 31, pp. 662–670.

Shi, X.J., Wang, T., Zhang, L., Castro, A., Xiao, X.C., Tong, Y., Zhang, J.J., Guo, L., and Yang, Q.D., Timing, petrogenesis and tectonic setting of the Late Paleozoic gabbro–granodiorite–granite intrusions in the Shalazhashan of northern Alxa: constraints on the southernmost boundary of the Central Asian Orogenic Belt, *Lithos*, 2014, 208–209, pp. 158–177.

Sun, S.S. and McDonough, W.F., Chemical and isotopic systematics of oceanic basalts: implications for mantle composition and processes, *Geol. Soc., London, Spec. Publ.,* 1989, vol. 42, pp. 313–345.

Sun, J., Liu, Z., Zhang, S., Li, X.G., and Qi, J.F., Large-scale removal of lithosphere underneath the North China Craton in the Early Cretaceous: geochemical constraints from volcanic lavas in the Bohai Bay Basin, *Lithos,* 2017, vol. 292–293, pp. 69–80.

Thirlwall, M.F., Smith, T.E., Graham, A.M., Theodorou, N., Hollings, P., Davidson, J.P., and Arculus, R.J., High field strength element anomalies in arc lavas: source or process? *J. Petrol.,* 1994, vol. 35, pp. 819–838.

Wang, T.Y., Wang, S.Z., and Wang, J.R., *The Formation and Evolution of Paleozoic Continental Crust in Alxa Region*, Lanzhou: Lanzhou University Press, 1994. (in Chinese).

Williams, I.S., Buick, A., and Cartwright, I., An extended episode of early Mesoproterozoic metamorphic fluid flow in the Reynold Region, central Australia, *J. Metamorph. Geol.,* 1996, vol. 14, pp. 29–47.

Windley, B.F., Alexeiev, D., Xiao, W.J., Kröner, A., and Badarch, G., Tectonic models for accretion of the Central Asian Orogenic Belt, *J. Geol. Soc. London,* 2007, vol. 164, pp. 31–47.

Wu, T.R., He, G.Q., and Zhang, C., On Paleozoic tectonics in the Alxa region, *Acta Geol. Sinica,* 1998, vol. 72, pp. 256–263.

Xiao, W.J., Windley, B.F., Huang, B.C., Han, C.M., Yuan, C., Chen, H.L., Sun, M., Sun, S., and Li, J.L., End-Permian to mid-Triassic termination of the accretionary processes of the southern Altaids: implications for the geodynamic evolution, Phanerozoic continental growth, and metallogeny of Central Asia, *Int. J. Earth Sci.,* 2009, vol. 98, no. 6, pp. 1189–1217.

Xiao, W.J., Windley, B., Sun, S., Li, J.L., Huang, B.C., Han, C.M., Yuan, C., Sun, M., and Chen, H.L., A tale of amalgamation of three Permo-Triassic collage systems in Central Asia: oroclines, sutures, and terminal accretion, *Annu. Rev. Earth Planet. Sci.,* 2015, vol. 43, no. 1, pp. 477–507.

Xu, X.S., Griffin, W.L., Ma, X., O'Reilly, S.Y., He, Z.Y., and Zhang, C.L., The Taihua group on the southern margin of the North China craton: further insights from U-Pb ages and Hf isotope compositions of zircons, *Mineral. Petrol.,* 2009, vol. 97, pp. 43–59.

Zhang, L., Shi, X.J., Zhang, J.J., Yang, Q.D., Tong, Y., and Wang, T., LA-ICP-MS zircon U-Pb age and geochemical characteristics of the Taohaotuoxiquan gabbro in northern Alxa, Inner Mongolia, *Geol. Bull. China,* 2013, vol. 32, pp. 1536–1547.

Zhang, X.R., Zhao, G.C., Eizenhöfer, P.R., Sun, M., Han, Y.G., Hou, W.Z., Liu, D.X., Wang, B., Liu, Q., and Xu, B., Paleozoic magmatism and metamorphism in the Central Tianshan block revealed by U–Pb and Lu–Hf isotope studies of detrital zircons from the South Tianshan belt, NW China, *Lithos,* 2015a, vol. 233, pp. 193–208.

Zhang, X.R., Zhao, G.C., Eizenhöfer, P.R., Sun, M., Han, Y.G., Hou, W.Z., Liu, D.X., Wang, B., Liu, Q., and Xu, B., Latest Carboniferous closure of the Junggar Ocean constrained by geochemical and zircon U–Pb-Hf isotopic data of granitic gneisses from the Central Tianshan block, NW China, *Lithos*, 2015b, vol. 238, pp. 26–36.

Zhao, J.H. and Zhou, M.F., Geochemistry of Neoproterozoic mafic intrusions in the Panzhihua district (Sichuan Province, SW China): implications for subduction related metasomatism in the upper mantle, *Precambrian Res.,* 2007, vol. 132, pp. 27–47.

Zheng, R.G., Wu, T.R., Zhang, W., Xu, C., Meng, Q.P., and Zhang, Z.Y., Late Paleozoic subduction system in the northern margin of the Alxa block, Altaids: geochronological and geochemical evidences from ophiolites, *Gondwana Res.,* 2014, vol. 25, no. 2, pp. 842–858.